Topological mixing of yield stress materials

D. R. Lester*
School of Engineering, RMIT University, 3000 Melbourne, Australia

A. Chryss
CSIRO Mineral Resources, Clayton, Victoria 3169, Australia

(Received 17 December 2018; published 14 June 2019)

We study the chaotic mixing of non-Newtonian fluids in a static mixing device based upon ideas from topological mixing. The kinematic and topological basis of this device means that fluid mixing and deformation is independent of the flow dynamics, facilitating rapid, global mixing of continuous media regardless of rheology and flow rate. Via experiments and computational studies, we demonstrate the efficacy of this device for a range of viscoplastic non-Newtonian materials, which are traditionally difficult to mix. We elucidate the governing principles upon which this device operates and gauge the scope for applications to a broad class of rheological materials.

DOI: 10.1103/PhysRevFluids.4.064502

I. INTRODUCTION

The mixing of yield stress fluids such as concentrated mineral slurries, colloidal gels and suspensions, emulsions, cosmetics and pharmaceutical products, and other highly concentrated, high-value formulations is central to a wide range of natural and engineered processes. Such viscoplastic materials are particularly challenging to effectively mix using conventional methods as their very high viscosity prevents the attainment of turbulent flow conditions in most practical settings. Even if turbulent mixing could be possible, it is highly inefficient, with mixing efficiency e (defined as the proportion of fluid deformations that result in persistent stretching) of conventional, turbulent mixers typically only a few percent [1]. Mixing methods such as chaotic advection [2,3] are well-suited to address these challenges, where mixing via a series of controlled, programed flows that are regular in the Eulerian frame can generate chaotic particle trajectories (Lagrangian chaos) and elongation of material elements that is exponential in time. Such chaotic advection corresponds to rapid mixing that is much more efficient; Khakhar and Ottino [4] show that the maximum stretching efficiency $e_{\max}$ of d-dimensional chaotic flows is given by $e_{\max} = \sqrt{d/(1-d)}$, and many chaotic flows achieve efficiencies in the range $e = 20$–$40\,\%$. Furthermore, Raynal and Gence [5] show that energy E required to mix chaotic Stokes flow and turbulent flow of the same fluid is given in terms of the Reynolds numbers Re as $E_{\text{Stokes}}/E_{\text{turbulent}} \approx \text{Re}_{\text{Stokes}}/(2\,\text{Re}^2_{\text{turbulent}})$. Hence chaotic mixing methods are well-suited to the processing of highly non-Newtonian materials [6].

However, mixing of yield stress fluids is particularly challenging as these materials have a tendency to yield plastically along highly localized slip planes (in a manner akin to purely plastic materials) rather than deforming smoothly and continuously. The building blocks of chaotic mixing are the stretching and folding (SF) motions of the fluid flow [2,3]; together these motions generate highly striated material distributions that rapidly homogenize in the presence of arbitrarily small diffusion. The discontinuous deformation inherent to yield stress materials can limit the efficacy

*daniel.lester@rmit.edu.au

of mixing strategies that are designed based upon SF protocols. Rather, discontinuously deforming materials can be effectively mixed using "cutting and shuffling" (CS) motions (characterized as piecewise isometries [7]), which use failure along slip planes to mix such materials in the same manner as the shuffling of a deck of cards [8,9]. Unlike granular media, yield stress materials can exhibit both SF and CS deformations. Smith et al. [10] have shown that a mixture of SF and CS motions can be used to impart rapid and effective mixing of discontinuously deforming media such as yield stress fluids.

A related yet distinct issue regarding yield stress fluids, especially multiphase fluids such as suspensions and emulsions, is their tendency to slip at solid boundaries. Such wall slip hinders the ability for boundary motions to control interior flow and deformation, and it can lead to discontinuous deformation in the interior [10,11]. Hence it is highly desirable to develop mixing approaches for yield stress fluids that are insensitive to wall slip. Another issue facing the practical design of mixing solutions for highly non-Newtonian and yield stress materials is that of rheological variability. Presently, many chaotic mixing devices (such as the rotated arc mixer [12,13], the partitioned pipe mixer [14,15], the SMX static mixer [16], and the herringbone mixer [17]) require knowledge of the material rheology for optimization of the mixing device parameters that effectively "program" the most efficient mixing protocol for the material at hand. This step is critical as a poor parameter choice can often lead to highly ineffective mixing. The mixing efficiency in chaotic mixers has been shown [6,13] to be fractally distributed across the mixing device parameter space, presenting a significant challenge for conventional optimization techniques. While the ability to tune the mixing protocol is highly desirable in many applications where the material rheology is known and fixed, in many processes (such as mineral and wastewater processing) the feed material rheology is unknown and/or highly variable due to upstream fluctuations. As such, there is a strong need to develop chaotic mixing strategies that provide robust, efficient mixing of yield stress materials across a broad range of rheology (from viscous- to plastic-dominated) and wall behavior (from no-slip to free-slip boundary conditions).

In this study, we explore the potential for a static mixing device that can address the multiple challenges associated with the chaotic mixing of yield stress materials. This device is inspired by recent studies on the mixing of fluids in porous media [18,19] and in a novel device, termed a *baker's flow* [20], which is a three-dimensional (3D) fluid mechanical analog of the baker's map, an archetypical 2D map used for the study of chaos in dynamical systems. As fluid flows along the device, the 3D baker's flow imparts similar motions (namely stretching and stacking of fluid elements) as is achieved in time as the 2D baker's map. As these motions are primarily driven by the underlying topology of the mixing device, we term this device a *topological mixer* (not to be confused with topological mixing achieved by the braiding motion of stirring rods in 2D flows [21,22]). Mixing is primarily driven by the basic topology of the device rather than the specific flow dynamics (which play a secondary role), leading to mixing that is significantly less dependent upon the material rheology than conventional chaotic mixing approaches.

To explore these concepts, we study the chaotic mixing of yield stress fluids with a range of different rheologies in a static mixer similar to the 3D baker's flow. We use a combination of experimental and numerical methods to study the flow, deformation, and mixing of these materials, and we examine the efficiency of the mixing process over the rheological spectrum under consideration. We examine in detail the mechanisms that control mixing of yield stress materials in Sec. II, followed by a description of the experimental and computational methods used in Sec. III. In Sec. IV, results and a discussion of observations are given, including elucidation of the governing principles and the scope of applicability of topological mixing methods to yield stress materials more broadly.

II. MECHANISMS OF MIXING OF YIELD STRESS MATERIALS

As outlined in the Introduction, yield stress materials are particularly challenging to mix due to (i) their inherent propensity to fail discontinuously along yield surfaces rather than deform smoothly

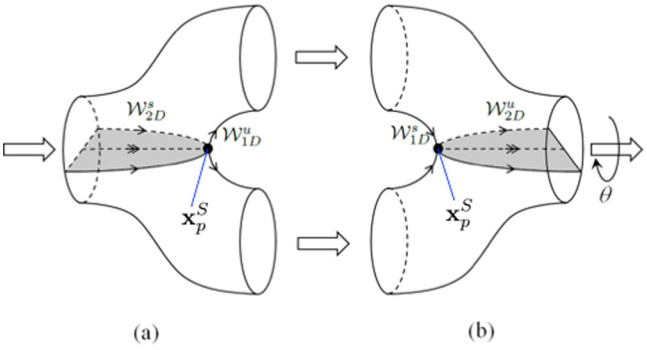

FIG. 1. Schematic of saddle point $\mathbf{x}_p^S$, 2D (1D) stable $\mathcal{W}^S_{2D}$ ($\mathcal{W}^S_{1D}$) and unstable $\mathcal{W}^U_{2D}$ ($\mathcal{W}^U_{1D}$) manifolds in a pore (a) branch and (b) merger. Adapted from [18].

and continuously, (ii) the large stresses required to invoke deformation and flow throughout the fluid domain, (iii) the large energy consumption associated with the attainment of turbulent flow, and finally (iv) the impracticalities associated with generating turbulence in such viscous-dominated materials. While chaotic advection is well-suited to address challenges (ii)–(iv), the first challenge requires approaches that go beyond the conventional stretching and folding route to chaos. Furthermore, many applications demand mixing solutions that can be applied to a wide range of rheologies, without the need for optimization of the mixing protocol. We shall first consider mixing approaches to address the latter problem (based on the assumption of continuous deformation of material), prior to consideration of how these approaches handle mixing of discontinuous deforming media.

A. Topological mixing of continuously deforming media

Topological mixers, which operate on the principle that topological complexity can generate efficient chaotic mixing, are well-suited to address this challenge as the detailed fluid dynamics and resultant flow kinematics play a secondary role to the bulk motions that are imparted by the device topology. As such, any deformable material (whether it deforms in a continuous, discontinuous, or mixed manner) that passes through these devices must undergo some persistent deformation due to the topology of the device, and this persistent deformation is often synonymous with that required for efficient, robust mixing.

The motivation for this class of topological mixers comes from the discovery [18] of the dominant mixing mechanism in porous media, namely that the topological complexity inherent in all porous media imparts chaotic mixing. Using the Poincaré-Hopf theorem, Lester et al. [18] show that the highly connected pores in porous media (as quantified by the topological genus g per unit volume) give rise to a large number density of saddle points $\mathbf{x}_p^S$ in the skin friction field $\mathbf{u} \equiv \partial \mathbf{v}/\partial x_3$ (where $\mathbf{v}$ is the fluid velocity and x_3 is the coordinate normal to the pore boundary) on the pore boundary. As shown in Fig. 1, these saddle points in a pore branch (a) or pore merger (b) (which are individually referred to as a topological "pair of pants" for obvious reasons) are directly responsible [23,24] for the formation of 2D separation and reattachment surfaces in the fluid interior (known as 2D stable $\mathcal{W}^S_{2D}$ and unstable $\mathcal{W}^U_{2D}$ manifolds), which undergo hyperbolic (exponential) fluid stretching. Due to this stretching, these 2D manifolds represent transport barriers that organize fluid transport and mixing, and they form what is termed the "skeleton of the flow" [24].

The topological complexity of the pore branch and merger in Fig. 1 is illustrated by gluing these elements together to form a single *mixing element*; the hole that forms in the middle of this mixing element means it has a topological genus g of 1 (the topological genus measures the number of handles or holes an object has, such that a sphere is of genus 0, a torus genus 1), and the genus of

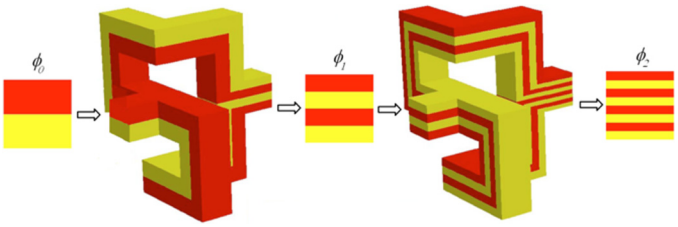

FIG. 2. Schematic of 3D baker's flow with evolution of colored fluid elements. Adapted from [20].

multiple mixing elements connected in series (or as part of a porous network) has a genus equal to the total number of mixing elements. This topological complexity—as quantified by the total number of holes—is directly responsible for the formation of saddle points $\mathbf{x}_p^S$ and, as shall be shown, chaotic mixing.

As the 2D stable and unstable manifolds, respectively, propagate upstream and downstream in the flow, these manifolds intersect when multiple pore branches and mergers shown in Fig. 1 are connected in series. For simplicity of exposition, we consider these manifolds as planar surfaces, and we use θ in Fig. 1 to denote the angle of intersection. If these stable and unstable manifolds connect smoothly ($\theta = 0$), the hyperbolic contraction of the former cancels the expansion in the latter, leading to zero net fluid deformation. Conversely, if the stable and unstable manifolds intersect transversely ($\theta \neq 0$), a so-called heteroclinic tangle ensues (the hallmark of chaos in continuous systems), leading to chaotic mixing of the fluid. As smooth connections only arise in exceptional, highly symmetric cases, chaotic mixing is the norm rather than the exception.

It is important to note that the formation of the 2D stable and unstable manifolds that generate chaotic mixing is completely independent of the pore geometry, boundary conditions (BCs), fluid mechanics, and rheology; rather, these structures are a direct consequence of the topological complexity of the pore space, and so they are inherent to all deformable media flowing through the pore space. Conversely, the nature of the intersection between the manifolds (i.e., smooth or transverse) is dependent upon the pore geometry, fluid mechanics, and rheology, and so in principle the mixing dynamics can vary with rheology and BCs in topological mixers. Despite this fact, we shall show that this variability can be rendered negligible by utilizing certain design rules to optimize mixing, essentially by ensuring that stable and unstable manifolds connect transversely. These rules arise from symmetry considerations that are largely independent of the fluid rheology (except in the case of viscoelastic materials, which are beyond the scope of this study) and BCs, facilitating the design of effective, robust topological mixers for yield stress materials.

While a random connection of pore branches and mergers [Figs. 1(a) and 1(b), respectively] has been used to construct 3D random and ordered pore networks and to study its transport properties [18,19,25,26], these elements can also be connected sequentially in an ordered fashion to form a longitudinal topological mixer in a manner similar to a traditional static mixer. The mixing efficiency of such a device for Newtonian fluids has been studied in [20], in which it was shown numerically that a sequence of branches and mergers, connected with an additional twist to ensure $\theta = \pi/2$, generates rapid, almost global chaotic mixing of a Newtonian fluid undergoing Stokes flow. As shown in Fig. 2, this device achieves a *baker's flow*, a 3D fluid mechanical analog of the *baker's map*. Here the cross section ϕ_i of a fluid material distribution after the ith mixing element depicts the stretching (by a factor of 2) and stacking of material elements that involve material striations that decrease in thickness as 2^{-i} and so must lengthen by 2^i via mass conservation. Although the baker's flow appears to achieve fluid stretching, cutting (which is not possible for continuously deforming media), and stacking of fluid elements when projected into the 2D plane (denoted by ϕ_i in Fig. 2) transverse to the mean flow, these apparent motions are actually achieved by a stretching and folding (SF) mixing protocol: stretching of fluid elements by the 2D stable and unstable manifolds, and folding of fluid elements due to flow over the saddle point (which is a stagnation).

The Poincaré section (not shown) for this flow indicates almost global mixing (with some small reentrant vortices in the mixer corners due to the finite Stokes number used in calculations). The Lyapunov exponent (scaled in terms of mixing element number i rather than time)

$$\lambda_\infty \equiv \lim_{i\to\infty} \frac{1}{i} \ln \frac{||\mathbf{l}(i)||}{||\mathbf{l}(0)||}, \tag{1}$$

where $\mathbf{l}(i)$ represents an infinitesimal material line vector at plane i that is measured to be $\lambda_\infty \approx 0.6$, which is about 98% of the theoretical maximum $\lambda_\infty = \ln 2$ for continuous systems. Similarly, it has been shown [18] that ordered pore networks with $\theta = \pi/2$ achieve global mixing with $\lambda_\infty = \ln 2$. As such, 3D baker's flows can impart very efficient, near-global chaotic mixing of continuously deforming media based on the topological complexity of the device.

B. Topological mixing of discontinuously deforming media

We now consider to what extent a topological mixer such as the 3D baker's flow can mix discontinuously deforming media. SF is fundamental to the mixing of smoothly deforming, continuous materials, but for discontinuously deforming materials (such as granular media) mixing can also be achieved by cutting and shuffling (CS) of material elements, similar to that of a deck of cards. While most flows of discontinuously deforming media involve a mixture of CS and SF [9,10,27,28], leading to highly efficient mixing, in this section we consider how well the 3D baker's flow can mix discontinuously deforming materials under CS only. The admission of cutting and shuffling motions has significant implications for fluid mixing. First, CS represents an extra degree of topological freedom that is not possible under smooth, continuous deformations, and so it encompasses additional mixing mechanisms. While both SF and CS can each lead to complete mixing in the sense that the interfacial area between parts of the material can grow without bounds, a fundamental difference is that CS does not involve material deformation. The Lyapunov exponent λ_∞ is positive in chaotic SF systems, leading to exponential rates of mixing, but it is identically zero in CS systems in which the mixing rate can only be algebraic. In the language of ergodic theory, SF can achieve strong mixing, whereas CS can only achieve weak mixing.

Discontinuous mixing via CS can be clearly understood in terms of "piecewise isometries" [7,9], which in 1D, 2D, or 3D can be considered as the different ways in which a collection of lines, areas, or volumes, respectively, may be cut out of a line, plane, or volume and then repositioned with different locations and or orientations to form a contiguous whole. Piecewise isometries have been used to understand how CS mixing occurs in, e.g., granular tumblers [8,9], microfluidic DNA microarrays [27], and pulsed flow systems [10,28]. Central to the dynamics of piecewise isometries is the concept of the *web of Lagrangian discontinuities*, which provide a template for the overall transport dynamics in CS systems. Here, the web of discontinuities is made up of all points where material will eventually experience a discontinuous deformation, and the web of images comprises points where the discontinuous deformations are advected into the fluid bulk.

In the context of topological mixers such as the 3D baker's flow, the basic topology of these devices ensures that discontinuously deforming materials such as granular media must undergo CS to be able to flow over, e.g., the branch and merger shown in Fig. 1. This deformation would involve a (possibly complex) set of slip lines and material orientations. If we now consider a sequence of pore branches and mergers in series, as long as there exists symmetry breaking (as given by $\theta \neq 0$ in Fig. 1) between successive elements (such that the slip lines, etc., do not coincide at all pore elements), then subsequent iterates of these deformations can become space-filling and hence mixing. As such, topological mixers certainly have the potential to engender complete "weak mixing" of discontinuously deforming media, although the rate, extent, and robustness of these mixing mechanisms is an open problem. It is also unknown to what extent topological mixers can impart efficient mixing of yield stress materials, which typically deform via a combination of SF (in the yielded regions) and CS (at the boundary of yield regions) deformations.

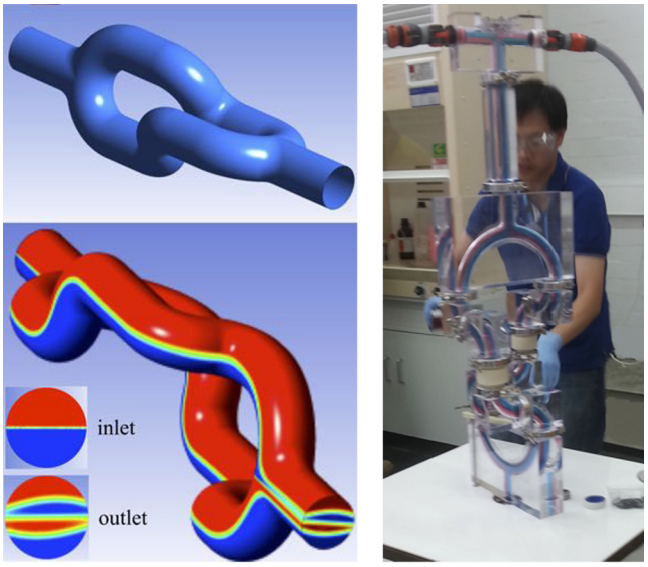

(a) (b)

FIG. 3. (a) (Top) Schematic of a topological mixing element with (bottom) typical scalar concentration distribution for flow of a yield stress fluid from numerical simulations. (b) Experimental embodiment of the topological mixing element (vertical orientation).

III. EXPERIMENTAL AND COMPUTATIONAL METHODS

To address these questions, we consider the flow of yield stress materials ranging from viscous-dominated to plastic-dominated fluids through a topological mixer that is based on the baker's flow formed by the pore branch and merger shown in Fig. 1, and the topological mixer considered by Carrieré [20] (Fig. 2). A schematic of the geometry of a mixer element is shown in Fig. 3(a), which consists of a pore branch and merger that are connected by twisted pipe sections to impart a reorientation angle of $\theta = \pi/2$ in a manner similar to that used by Carrieré [20]. For practical reasons we use rounded pipe sections, and the pipe sections that connect the pore branch and merge elements in the 3D baker's flow (Fig. 2) have been extended to suppress the rotation of yield stress fluids as they flow through the mixer. Such rotation reduces the effective orientation angle θ, lowering the efficiency of the device. As shown in Fig. 3(a), this mixing element generates layering of fluid elements in a similar manner to that of the 3D baker's flow (Fig. 2).

A topological mixer is then formed by connecting several mixing elements together to yield an elongated mixer similar to a conventional static mixer. It is interesting to note that conventional static mixers are also topologically complex in that there exists a high number density of handles in the flow domain. However, conventional static mixers typically require a prohibitively large driving pressure for yield stress fluids due to the small flow apertures. We shall use a combination of experimental and numerical methods to study the flow and mixing mechanisms of yield stress fluids through this device, and determine the mixing robustness and efficiency across a range of rheology and BCs.

To experimentally test the topological mixer shown in Fig. 3(a), we constructed an experimental embodiment of a single mixing element [see Fig. 3(b)] that consists of 30 mm ID Perspex sections to facilitate direct visualization of the flow and deformation of dyed, optically clear working fluids. While it was not possible to construct a device with the same geometry as the mixing element in Fig. 3(a) that allowed visualization of the mixing behavior, this experimental rig provides valuable data for validation against numerical simulations. Transparent viscoplastic test fluids were generated

TABLE I. Herschel-Bulkley parameters for the experimental test fluids.

Fluid	τ_y (Pa)	k (Pa s^n)	n (−)	Dye
T1	29.3	13.1	0.38	Brilliant Blue
T2	23.0	9.50	0.40	Armoisine
T3	0.10	0.389	0.54	Dilute Brilliant Blue
T4	0.01	0.120	0.66	Dilute Armoisine

by dyeing pH neutralized Carbopol with 5 ppm by mass of red dye (Armoisine: Ravicol Carmoisine RA3003) and blue dye (Brilliant Blue: Brilliant Blue FCF RA5001), respectively, to experiments fluids T1 and T2, which had slightly different rheological properties due to the different dyes used. Two more experimental fluids, T3 and T4, were made up by diluting one part of fluids T1 and T2, respectively, with two parts water, resulting in less viscous fluids. All four solutions were rheologically characterized with a Couette rheometer. The dyed Carbopol solutions displayed no significant viscoelastic effects. As summarized in Table I, the rheology of all of these test fluids is well described by a Herschel-Bulkley viscoplastic model

$$\begin{aligned} \dot{\gamma} &= 0, & \tau &< \tau_y, \\ \tau &= \tau_y + \kappa \dot{\gamma}^n, & \tau &\geqslant \tau_y, \end{aligned} \tag{2}$$

where $\dot{\gamma}$ is the shear rate, τ is the shear stress, τ_y is the yield stress, κ is the consistency, and n is the flow index.

The experimental fluids T1–T4 are used for four different experimental runs summarized in Table II; these experiments involve two experiments under creep flow conditions ($\mathrm{Re} \leqslant 0.1$) and two under laminar flow conditions ($0.1 < \mathrm{Re} \leqslant 10$), with negligible Dean numbers Dn in all cases. The two pairs of two different colored fluids with similar rheology (T1 and T2, T3, and T4) were injected via two peristaltic pumps at equal flow rates into a baffled feed section [Fig. 5(a)], and images of the mixing at various stages (Fig. 4) and the output (Fig. 5) were recorded. The high-yield stress of fluids T1 and T2 allowed the rig to be dismantled and a cross section imaged [Fig. 6(b)].

Numerical simulation of the steady flow and mixing of Herschel-Bulkley fluids in the topological mixer were performed by solving the incompressible Navier-Stokes (NS) equations for the velocity field $\mathbf{v}(\mathbf{x})$ and an advection-diffusion equation (ADE) for the scalar field $\phi(\mathbf{x})$ in the fluid domain $\mathcal{D}$, subject to zero penetration and homogeneous Neumann BCs on the fluid boundary $\partial\mathcal{D}$,

$$\boldsymbol{\nabla} \cdot \mathbf{v} = \mathbf{0}, \tag{3}$$

$$\rho \mathbf{v} \cdot \boldsymbol{\nabla} \mathbf{v} = -\boldsymbol{\nabla} p + \boldsymbol{\nabla} \cdot \boldsymbol{\tau} + \rho \mathbf{g}, \quad \mathbf{v} \cdot \mathbf{n}\big|_{\partial\mathcal{D}} = \mathbf{0}, \tag{4}$$

$$\mathbf{v} \cdot \boldsymbol{\nabla} \phi = D_m \nabla^2 \phi, \quad \boldsymbol{\nabla} \phi \cdot \mathbf{n}|_{\partial\mathcal{D}} = \mathbf{0}. \tag{5}$$

In (3)–(5), ρ is the fluid density, p is the pressure, $\boldsymbol{\tau}$ is deviatoric stress, $\mathbf{g}$ is gravitational acceleration, $\mathbf{n}$ is the outward unit vector normal to the boundary $\partial\mathcal{D}$, and D_m is the molecular

TABLE II. Flow rates and dimensionless groups for all runs.

Run	Fluids	Q (L/min)	Re	De
1	T1, T2	0.5	0.01	0.0003
2	T1, T2	2	0.1	0.003
3	T3, T4	0.5	0.5	0.01
4	T3, T4	2	4.0	0.1

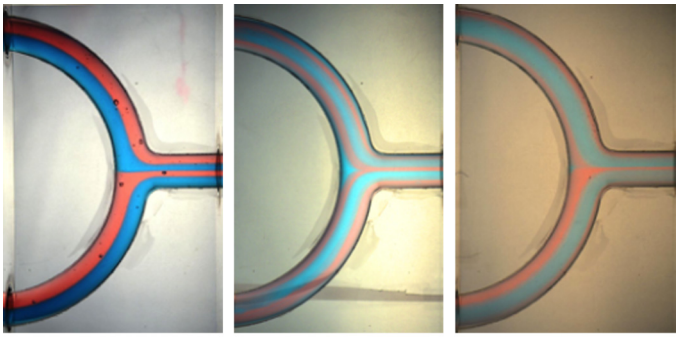

(a) (b) (c)

FIG. 4. Fluid distribution in upper U-bend of the experimental topological mixer for (a) Runs 1 and 2, (b) Run 3, and (c) Run 4.

diffusivity of the scalar field ϕ, which corresponds to a Peclét number of 10^5. To test the impact of different shear BCs, we consider either no-slip or free-slip BCs,

$$\mathbf{v} \cdot \mathbf{n}\big|_{\partial\mathcal{D}} = \mathbf{0}, \tag{6}$$

$$\mathbf{t} \cdot \boldsymbol{\tau} \cdot \mathbf{n}\big|_{\partial\mathcal{D}} = \mathbf{0}, \tag{7}$$

where $\mathbf{t}$ is an arbitrary unit vector tangential to the boundary $\partial\mathcal{D}$. Periodic conditions for the fluid velocity were applied at the mixing element inlet and outlet, and the flow was driven using a uniform pressure gradient that results in a volumetric flow rate of 0.277 $\mathrm{m}^3\ \mathrm{s}^{-1}$. The inlet conditions for the scalar concentration field consist of two semicircular regions of concentration $\phi = 1$ and 0 as shown in Fig. 3. As the Herschel-Bulkley rheology (2) results in a singular viscosity in unyielded regions where the shear rate $\dot{\gamma} = 0$, following the method of Bercovier and Engelman [29], we regularize

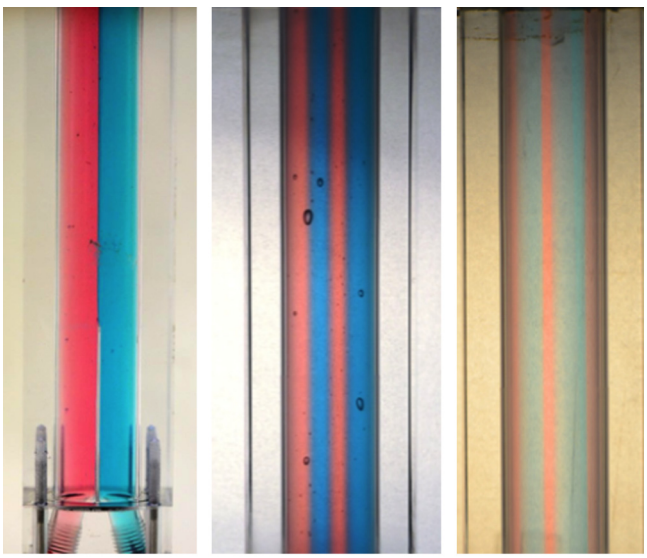

(a) (b) (c)

FIG. 5. Fluid distribution for (a) inlet and (b) outlet for Runs 1 and 2, and (c) outlet for Run 3.

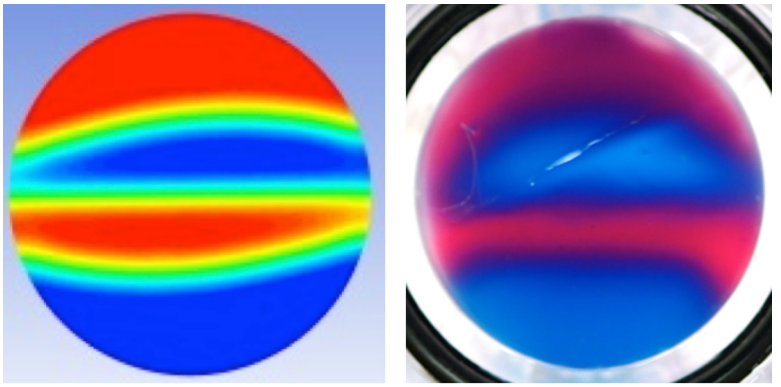

(a) (b)

FIG. 6. Comparison of dye distribution for mixing of fluids T1 and T2 from (a) numerical simulations and (b) experiments over a single mixing element.

this viscosity via the limiting minimum shear rate of $\dot{\gamma}_0 = 10^{-6}$ s^{-1} such that the non-Newtonian viscosity $\eta(\dot{\gamma})$ is approximated as

$$\boldsymbol{\tau} = 2\eta_{\text{eff}}(\dot{\gamma})\boldsymbol{\epsilon}, \;\; \boldsymbol{\epsilon} = \tfrac{1}{2}(\boldsymbol{\nabla}\mathbf{v} + \boldsymbol{\nabla}\mathbf{v}^{\top}), \;\; \dot{\gamma} = \sqrt{2\boldsymbol{\epsilon} : \boldsymbol{\epsilon}}, \tag{8}$$

$$\eta_{\text{eff}}(\dot{\gamma}) = \begin{cases} \frac{\tau_y}{\dot{\gamma}_0} + \kappa\dot{\gamma}_0^{n-1}, & \dot{\gamma} < \dot{\gamma}_0, \\ \frac{\tau_y}{\dot{\gamma}} + \kappa\dot{\gamma}^{n-1}, & \dot{\gamma} \geqslant \dot{\gamma}_0. \end{cases} \tag{9}$$

The governing equations were solved using the vertex centered finite volume CFD code ANSYS-CFX 14.5, via a third-order QUICK advection scheme and a SIMPLE pressure-velocity coupling algorithm. All solutions were iterated until all residuals achieved a rms value of less than 10^{-8}. A mesh refinement study found that a fine mesh with characteristic grid size $\Delta x = 0.2$ mm, comprising over 3.7 million elements per mixing element, was sufficient to fully resolve the flow and yield regions, and the flow over each bend was solved sequentially over 20 bends to reduce memory overhead. In addition to the experimental HB fluids, the mixing of eight additional HB fluids (R1–R8, summarized in Table III), which correspond to maxima and minima of yield stress τ_y, consistency k, and flow index n, spans a wide range of yield stress materials relevant to many industrial applications. These cases range from viscous-dominated ($\tau_y = 15$ Pa, $k = 5$ Pa s^n) to plastic-dominated ($\tau_y = 50$ Pa, $k = 0.1$ Pa s^n) yield stress fluids, and from strongly ($n = 0.3$) to

TABLE III. Herschel-Bulkley parameters for fluids R1–R8.

Fluid	τ_y (Pa)	n (−)	k (Pa s^n)
R1	15	0.3	0.1
R2	15	0.3	5
R3	15	0.9	0.1
R4	15	0.9	5
R5	50	0.3	0.1
R6	50	0.3	5
R7	50	0.9	0.1
R8	50	0.9	5

weakly ($n = 0.9$) shear-thinning rheologies, hence these fluids vigorously test the variability of mixing across a range of yield stress fluids in the topological mixer.

IV. RESULTS AND DISCUSSION

The dye distributions at the inlet and outlet and upper U-bend of the experimental topological mixer for Runs 1–4 are shown in Figs. 4 and 5; note that the results for Runs 1 and 2 are identical, indicating that variation of fluid deformation within the creep flow regime is negligible. Runs 1 and 2 show the effects of high-yield stress and vanishing Reynolds number with no mixing or secondary flow in the bends or inlet, but the outlet stream [Fig. 4(a)] clearly shows layering of the dyed fluids in the same manner as the 3D baker's flow (Fig. 2). The cross section of the outlet dye distribution for Runs 1 and 2 shown in Fig. 6(c) further confirms that the topological mixer is capable of producing layering of fluid elements similar to that of a 3D baker's flow for yield stress-dominated materials, and the gross mixing dynamics appear to be similar to that of continuously deforming media. While there is some minor distortion of the exit dye distribution [Fig. 6(b)] compared with the horizontal bands shown in the schematic in Fig. 2, these distortions do not affect the mixing dynamics in any material way. For the less viscous fluids (T3 and T4), similar behavior was observed in Run 3, where layering of the dye layers in Fig. 4(b) is similar to that of Runs 1 and 2, however evidence of weak Dean rolls (via twisting of dye fluid layers) is apparent in the lower U-bend in Fig. 4(b), despite the very low Reynolds ($\mathrm{Re} = 0.5$) and Dean ($\mathrm{De} = 0.01$) numbers. These secondary flows may be attributed to the absence of a significant yield stress for fluids T3 and T4 (Table I), and they are even more pronounced in Run 4, where the higher Reynolds ($\mathrm{Re} = 4$) and Dean ($\mathrm{De} = 0.1$) numbers produce more pronounced mixing [Fig. 4(c)] in addition to the topological mixing mechanism. These results confirm that topological mixers have the potential to effectively mix yield stress fluids in the creep flow regime, transition to weakly laminar flows and purely viscous materials, and then further accelerate mixing via the onset of secondary flows.

To probe the mixing characteristics of yield stress-dominated fluids in the creep regime, we first performed numerical simulations of the experimental fluids for Runs 1–4 in the experimental rig geometry to compare model predictions against experimental results. Figure 6 shows that the predicted dye distribution at the mixer outlet for Runs 1 and 2 agrees quite well with the experimental observations. While this visual comparison does not act as a robust validation per se, these results indicate that the CFD simulations are able to capture the gross flow and deformation in the experimental rig. We also note that the sectioning of the yield stress fluid to obtain Fig. 6(b) may have distorted the dye cross section to a minor degree. Based on this comparison, we then computed numerical simulations of mixing of fluids R1–R8 subject to both no-slip and free-slip BCs in a topological mixer comprised of 30 mixing elements [Fig. 3(a)] connected in series. The evolution of the scalar concentration field in the inlet plane for fluid R8 with no-slip BCs is shown in Fig. 7 (top), which illustrates rapid mixing in the central region of the inlet plane but weak mixing at the top and bottom regions. In an attempt to migrate these unmixed fluid elements into the central mixing region of the flow and produce global mixing, we introduce an angular reorientation between successive mixing elements given by the so-called "twist angle" χ. The resultant scalar concentration field for a twist angle of $\pi/2$ is shown in Fig. 7 (bottom), indicating mixing of these top and bottom regions, but large unmixed islands appear to persist, corresponding to a slower overall mixing rate.

This behavior is also reflected in the advection of nondiffusive tracer particles for fluid R8 subject to free-slip BCs shown in Fig. 8 for (top row) $\chi = 0$ and (bottom row) $\chi = \pi/4$. Similar to the scalar concentration fields for the no-slip BCs shown in Fig. 7, the twist angle $\chi = \pi/2$ acts to introduce large nonmixing islands into the flow, which never mix with the surrounding fluid. Conversely, the slow mixing regions at the top and bottom of the cross sections shown in the top row of Fig. 7 for the no-twist mixer (i.e., $\chi = 0$) do eventually mix. This behavior persists across all fluid rheologies and BCs; complete mixing is eventually achieved for the nonreoriented flow $\chi = 0$, but the introduction of the twist angle $\chi = \pi/4$ results in partial mixing in the flow domain with the presence of large, persistent nonmixing islands.

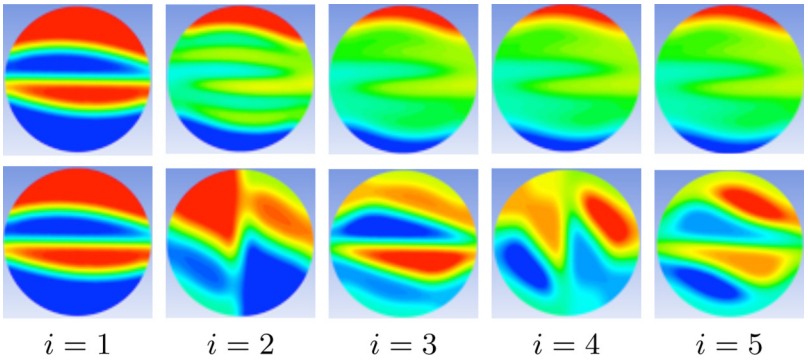

FIG. 7. Evolution of scalar concentration field with number i of mixing elements for fluid R8 subject to no-slip BCs in the (top) straight ($\chi = 0$) and (bottom) twisted ($\chi = \pi/2$) topological mixer.

To quantify the mixing dynamics in the topological mixer across the range of different fluid rheologies, BCs, and twist angles, we calculate the Lyapunov exponent λ_∞, scalar dissipation rate χ, and the mixing efficiency $e \in [0, 1]$, which measures the proportion of viscously dissipated energy that results in elongation of fluid elements as

$$e \equiv \left\langle \frac{\sqrt{2}}{\dot{\gamma}} \frac{\dot{\ell}}{\ell} \right\rangle, \tag{10}$$

where $\langle\rangle$ denotes an ensemble average over all trajectories, and ℓ is the length stretch of a line element

$$\ell \equiv \lim_{||d\mathbf{x}_0|| \to 0} \frac{||d\mathbf{x}||}{||d\mathbf{x}_0||}, \tag{11}$$

where $d\mathbf{x}$ is a material line element with initial orientation $d\mathbf{x}_0$. The evolution of such a line element is given in terms of the deformation gradient tensor $\mathbf{F}(t)$ as

$$d\mathbf{x}(t) = \mathbf{F}(t) \cdot d\mathbf{x}_0, \tag{12}$$

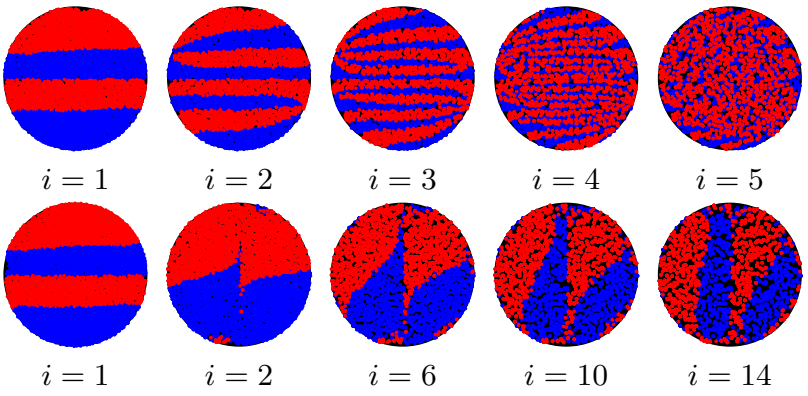

FIG. 8. Evolution of red and blue nondiffusive tracer particles with number i of mixing elements for fluid R8 subject to free-slip BCs in the (top) straight ($\chi = 0$) and (bottom) twisted ($\chi = \pi/2$) topological mixer.

TABLE IV. Mixing rate ξ, Lyapunov exponent λ_∞, and mixing efficiency e for fluids R1–R8 subject to no-slip BCs and different twist angle χ, within the topological mixer.

Fluid	χ	ξ	λ_∞	e	χ	ξ	λ_∞	e
R1	0	0.298	0.644	0.326	$\pi/2$	0.137	0.311	0.297
R2	0	0.282	0.610	0.287	$\pi/2$	0.141	0.293	0.292
R3	0	0.299	0.625	0.319	$\pi/2$	0.137	0.302	0.298
R4	0	0.291	0.517	0.324	$\pi/2$	0.141	0.288	0.302
R5	0	0.298	0.626	0.330	$\pi/2$	0.138	0.313	0.298
R6	0	0.289	0.485	0.325	$\pi/2$	0.141	0.226	0.294
R7	0	0.304	0.631	0.337	$\pi/2$	0.137	0.304	0.298
R8	0	0.297	0.476	0.325	$\pi/2$	0.139	0.257	0.295

where $\mathbf{F}(t)$ evolves in the Lagrangian frame as

$$\frac{d\mathbf{F}}{dt} = [\nabla \mathbf{v}]^\top \cdot \mathbf{F}(t), \;\; \mathbf{F}(0) = \mathbf{I}, \tag{13}$$

where t denotes the travel time along a particle trajectory. Combining (10)–(13) shows that the mixing efficiency measures the proportion of total fluid deformation that elongates fluid elements as

$$e = \left\langle \frac{1}{\sqrt{\boldsymbol{\epsilon} : \boldsymbol{\epsilon}}} \frac{d\mathbf{x}_0 \cdot \mathbf{F}^\top \cdot \boldsymbol{\epsilon} \cdot \mathbf{F} \cdot d\mathbf{x}_0}{d\mathbf{x}_0 \cdot \mathbf{F}^\top \cdot \mathbf{F} \cdot d\mathbf{x}_0} \right\rangle, \tag{14}$$

and the ensemble average also includes an average over all initial line element orientations $d\mathbf{x}_0$. We also use the deformation tensor $\mathbf{F}(t)$ over multiple particle trajectories to compute the Lyapunov exponent λ_∞ [rather than use (1) directly]

$$\lambda_\infty = \lim_{t \to \infty} \left\langle \frac{T}{2t} \ln \nu(t) \right\rangle, \tag{15}$$

where T is the mean residence time of fluid trajectories in the mixing element, and $\nu(t)$ is the largest eigenvalues of the Cauchy-Green tensor $\mathbf{C}(t) \equiv \mathbf{F}(t)^\top \cdot \mathbf{F}(t)$. It is important to note that the ensemble average in (15) represents a global average over all of the flow domain, such that the Lyapunov exponent λ_∞ is an area-weighted average over all topologically distinct regions of the Lagrangian flow field. This means that a partially chaotic flow (such as the flow with a twist angle $\chi = \pi/2$ shown in Fig. 8) that is comprised of chaotic regions (where the Lyapunov exponent is positive) and KAM islands (where the Lyapunov exponent is zero) has a mean Lyapunov exponent λ_∞ that is positive. As such, the quoted Lyapunov exponents in Tables IV and V must be interpreted with care as the cases for which $\chi = \pi/2$. There are regions that never mix or exchange material in the limit of vanishing diffusivity. It is for this reason that the scalar dissipation rate ξ differs strongly between the twist ($\chi = \pi/2$) and no-twist ($\chi = 0$) versions of the topological mixer, while the quoted Lyapunov exponents only vary moderately.

We also computed the scalar variance σ_i^2 of the concentration distribution $\phi_i(\mathbf{x})$ at the outlet of the ith mixing element

$$\sigma_i^2 = \frac{\int_A [\phi_i(\mathbf{x}) - \langle\phi\rangle]^2 dA}{\int_A [\phi_0(\mathbf{x}) - \langle\phi\rangle]^2 dA}, \tag{16}$$

where A is the cross-sectional area at the outlet and $\langle\phi\rangle$ is the mean concentration distribution at the inlet. As such, the variance σ_i evolves from the initial state $i = 1$ to the fully mixed state $i = 0$. Chaotic mixing imparts asymptotic exponential decay of scalar variance, hence we define the mixing

TABLE V. Twist angle χ, mixing rate ξ, Lyapunov exponent λ_∞, and mixing efficiency e for fluids R1–R8 subject to free-slip BCs within the topological mixer.

Fluid	χ	ξ	λ_∞	e	χ	ξ	λ_∞	e
R1	0	0.265	0.474	0.351	$\pi/2$	0.0597	0.194	0.341
R2	0	0.370	0.436	0.360	$\pi/2$	0.0967	0.187	0.344
R3	0	0.265	0.451	0.350	$\pi/2$	0.0531	0.114	0.339
R4	0	0.376	0.449	0.362	$\pi/2$	0.0956	0.127	0.339
R5	0	0.265	0.410	0.357	$\pi/2$	0.0533	0.116	0.346
R6	0	0.262	0.427	0.347	$\pi/2$	0.0492	0.126	0.348
R7	0	0.263	0.448	0.357	$\pi/2$	0.0455	0.122	0.340
R8	0	0.272	0.421	0.349	$\pi/2$	0.0371	0.117	0.344

rate ξ in the limit of large i as

$$\xi = \lim_{i\to\infty} \frac{1}{2i} \ln \frac{\sigma_i^2}{\sigma_0^2}. \tag{17}$$

Evolution of the scalar variance toward the exponential regime is illustrated by the straight lines in the large i limit for all cases in Fig. 9, where the response for small i is due to the decay of faster decaying eigenmodes associated with the initial condition, and the exponential regime indicates dominance of the slowest-decaying eigenmode that controls mixing.

Figure 9 and Tables IV and V show that the mixing rate ξ, Lyapunov exponent λ_∞, and mixing efficiency e across the fluids R1–R8 are remarkably similar, although there exist significant differences between mixing based upon the wall boundary condition and the twist angle. As indicated in Fig. 7, the nonzero twist angle ($\chi = \pi/2$) results in slower mixing as this represents a deviation from the optimal mixing condition $\theta = \pi/2$ as predicted by Lester et al. [18], resulting in the unmixed regions observed in Fig. 7 (bottom). This corresponds to a significantly lower scalar

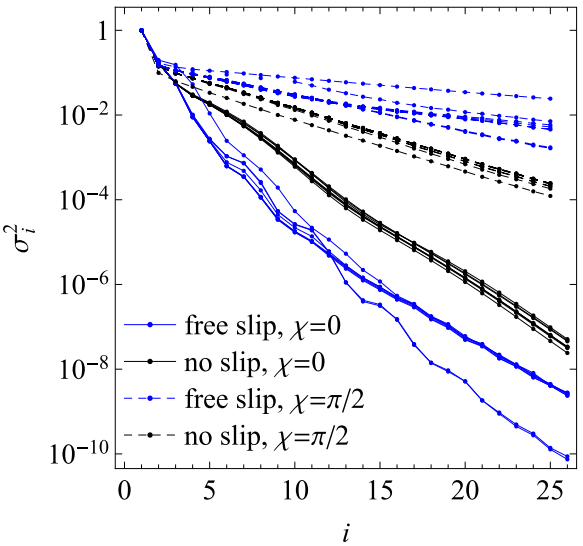

FIG. 9. Evolution of mixing index σ_i with number i of mixing elements for fluids R1–R8 in $\chi = 0$ and $\chi = \pi/2$ topological mixers under free-slip and no-slip BCs.

dissipation rate, Lyapunov exponent, and mixing efficiency. Henceforth we shall focus on the zero twist angle ($\chi = 0$) topological mixer.

Under no-slip BCs, the mean Lyapunov exponent λ_∞ for fluids R1–R8 is 85% of the theoretical maximum ln 2, and the variance of λ_∞ over these fluids is only 0.96% of this mean value. As such, the topological mixer is capable of robustly and efficiently mixing yield stress fluids subject to no-slip BCs, where a combination of wall shear and topological complexity results drives rapid, complete mixing. The distribution of mixing efficiencies e over these eight fluids is also closely centered about the mean value of $e = 0.321$, which is significantly higher than the maximum mixing efficiency for the random shear flow ($e = 0.284$) and the blinking vortex flow ($e = 0.166$). The mixing rate ξ is also very uniform across the eight fluid rheologies under no-slip BCs, where rapid decay toward homogeneity is observed in all cases.

Under free-slip BCs the mixing rate, mixing efficiency, and Lyapunov exponent in Table V vary slightly more across fluids R1–R8 than the no-slip case, but they are still fairly tightly bound. As illustrated in Fig. 9, fluids R2 and R4 have a significantly faster mixing rate ξ than the remaining fluids, which all mix at a very similar rate. Fluids R2 and R4 are characterized by the smallest relative yield stress (normalized by consistency), $\tau_y/k = 3s^{-n}$, and so they are most similar to a Newtonian fluid and thus mix faster than their high yield stress counterparts. Such a dependence of the mixing rate on relative yield stress is not observed for the no-slip fluids as the yield stress is overcome by wall shear everywhere on the fluid boundary. The average Lyapunov exponent is significantly small, with a mean that is 64% of the theoretical maximum ln 2, and the variance is only 0.14% of this value. This reduction in stretching rate is attributed to the absence of wall shear in this case, hence all fluid deformation is generated by the geometry of the topological mixer. This is also reflected by a reduction in the mean mixing rate ($\xi = 0.28$) over all eight fluids, however we note from Fig. 9 that the initial mixing rate under free-slip flow is significantly faster. While the free-slip conditions result in a lower Lyapunov exponent and asymptotic mixing rate, the mixing efficiency is significantly larger ($e = 0.354$) than under the no-slip conditions due to the absence of wall shear. As such, while wall shear contributes significantly to the flow resistance of yield stress fluids in the topological mixer, it only has a marginal effect on the mixing rate and so negatively impacts mixing efficiency. As such, the topological mixer can also achieve rapid, robust, and efficient mixing of yield stress materials that exhibit free wall slip. While not simulated, we assume that the many yield stress fluids (suspensions, emulsions, slurries, etc.) that exhibit partial wall slip also exhibit mixing characteristics in the topological mixer that lie between those of free-slip and no-slip fluids.

The shear rate distribution for fluid R8 under no-slip BCs shown in Fig. 10(a) indicates the presence of a low but finite shear rate region (i.e., $\dot{\gamma} > \dot{\gamma}_0$) in the vicinity of the stagnation point $\mathbf{x}_p^S$, corresponding to smoothly deforming flow. While discontinuous deformation is inherent to yield stress materials and there are large shear rate gradients within the flow, all of these deformations are continuous (in the limit of vanishing $\dot{\gamma}_0$), indicating that the predominant mixing mechanism within the topological mixer is SF rather than CS. Furthermore, the topology of the skeleton of the flow [given by the 1D unstable $\mathcal{W}^u_{1D}$ and 2D stable $\mathcal{W}^s_{2D}$ manifolds shown in Fig. 10(a)] is the same as that for a Newtonian fluid shown in Fig. 1(a), indicating the same basic mixing mechanism. As expected, the maximum shear rate for the no-slip BCs occurs at the walls of the topological mixer, and the shear rate forms a local minimum at the stagnation point $\mathbf{x}_p^S$. Conversely, the shear rate distribution for the free-slip fluid shows that fluid deformation is highly localized around the stagnation point $\mathbf{x}_p^S$, and there is negligible deformation away from this region, i.e., fluid deformation is driven by flow over the junction rather than wall shear. The skeleton of the flow under free-slip conditions also matches that of the Newtonian case shown in Fig. 1(a). Although not shown, this general behavior of both the no-slip and free-slip fluids extends to all rheological fluids R1–R8, and in all cases similar structures occur around the downstream separation saddle point.

The skin friction field for fluid R8 subject to no-slip BCs in the vicinity of a (downstream) separation saddle point $\mathbf{x}_p^S$ is shown in Fig. 11(a), which, in combination with Fig. 10(a), indicates that the flow skeleton has the same structure and topology as that for a Newtonian fluid shown in Fig. 1. The introduction of free-slip BCs significantly alters the skin friction field $\mathbf{u}(\mathbf{x})$. If we express

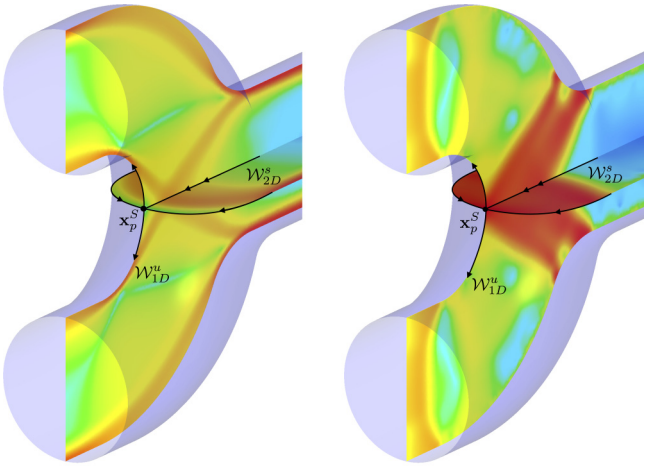

(a) (b)

FIG. 10. Shear rate distribution $\dot{\gamma}$ (log-scale) of fluid R8 in the vicinity of an attachment saddle point $\mathbf{x}^S_p$ in the topological mixing element subject to (a) no-slip and (b) free-slip BCs. Also shown are the 1D unstable $\mathcal{W}^u_{1D}$ and 2D stable $\mathcal{W}^s_{2D}$ manifolds. Red indicates the maximum shear rate ($\dot{\gamma} = 432.7$ and $101.2\ \mathrm{s}^{-1}$ under the no-slip and free-slip conditions, respectively) and blue indicates unyielded flow $\dot{\gamma} = \dot{\gamma}_0$.

the velocity field $\mathbf{v} = (v_1, v_2, v_3)$ in local coordinates $\mathbf{x} = (x_1, x_2, x_3)$, where x_1, x_2 are tangential to the boundary $\partial\mathcal{D}$, and x_3 is normal to $\partial\mathcal{D}$, then the unit vectors normal and tangential to $\partial\mathcal{D}$ can be expressed, respectively, as $\mathbf{n} = \mathbf{e}_3$, $\mathbf{t} = t_1\mathbf{e}_1 + t_2\mathbf{e}_2$, where the real, arbitrary scalars t_1 and t_2 satisfy $t_1^2 + t_2^2 = 1$. The free-slip boundary condition (7) may then be expressed as

$$\mathbf{t}\cdot\boldsymbol{\epsilon}\cdot\mathbf{n}\big|_{\partial\mathcal{D}} = \frac{t_1}{2}\frac{\partial v_1}{\partial x_3}\bigg|_{\partial\mathcal{D}} + \frac{t_2}{2}\frac{\partial v_2}{\partial x_3}\bigg|_{\partial\mathcal{D}} = 0, \tag{18}$$

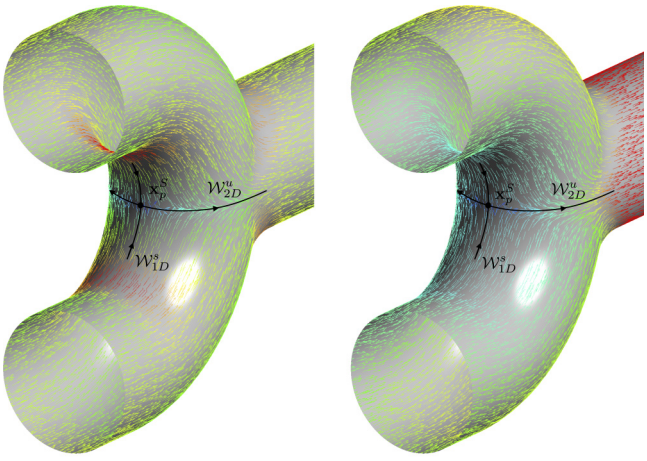

(a) (b)

FIG. 11. (a) Skin friction vector field $\mathbf{u}$ and (b) boundary velocity field $\mathbf{v}$ for fluid R8 in the vicinity of a downstream separation saddle point $\mathbf{x}^S_p$ on the fluid boundary $\partial\mathcal{D}$ of the topological mixer subject to (a) no-slip and (b) free-slip BCs.

which renders the (1,2) components of the skin friction field zero, as

$$\mathbf{u} \equiv \frac{\partial \mathbf{v}}{\partial x_3}|_{\partial\mathcal{D}} = \nabla\mathbf{v}\cdot\mathbf{n}|_{\partial\mathcal{D}} = \left(0, 0, \frac{\partial v_3}{\partial x_3}\right). \tag{19}$$

Hence the free-slip boundary condition renders the skin friction components that are tangential to the boundary zero. Conversely, the boundary velocity $\mathbf{v}|_{\partial\mathcal{D}}$ is nonzero under free-slip conditions, hence flow separation is governed by stagnation points $\mathbf{x}_p$ of the boundary velocity field $\mathbf{v}(\mathbf{x}_p) = \mathbf{0}$. Choosing x_1, x_2 to align with the tangential stretching directions around a stagnation point $\mathbf{x}_p$ renders the velocity gradient diagonal, which may then be linearized as

$$\nabla\mathbf{v} = \begin{pmatrix} v_{1,1} & 0 & 0 \\ 0 & v_{2,2} & 0 \\ 0 & 0 & v_{3,3} \end{pmatrix} \approx \begin{pmatrix} \lambda_1 & 0 & 0 \\ 0 & \lambda_2 & 0 \\ 0 & 0 & -\lambda_1 - \lambda_2 \end{pmatrix}. \tag{20}$$

Hence a stagnation point $\mathbf{x}_p$ corresponding to $\mathbf{v}(\mathbf{x}_p) = \mathbf{0}$ is of node $\mathbf{x}_p^N$ or saddle $\mathbf{x}_p^S$ type, respectively, depending upon whether λ_1 and λ_2 have the same or different signs. As for no-slip BCs, the Poincaré-Hopf theorem predicts a large number density of saddle points $\mathbf{x}_p^S$ (now in the boundary velocity field $\mathbf{v}$) for topologically complex domains, which again give rise to separation and reattachment surfaces. As such, saddle points and associated 2D stable $\mathcal{W}_{2\mathrm{D}}^S$ and unstable $\mathcal{W}_{2\mathrm{D}}^U$ manifolds also form in topologically complex domains with free-slip BCs, hence efficient mixing is also possible for yield stress materials that undergo slip at bounding walls. As reflected by the linearization in (20) and shown in Fig. 10(b), the local velocity gradient around the saddle point x_p^S is remarkably similar to that of a topological mixer with no-slip BCs [Fig. 10(a)]. This behavior is attributed to the fact that flow separation in the topological mixer is driven by the pressure gradient associated with flow impingement rather than shear arising from the skin friction field. This property then renders the mixing dynamics insensitive to the fluid BCs, which is critical to successful mixing of yield stress fluids. As for the no-slip BC case, fluid deformation occurs in a smooth, continuous manner without unyielded regions $\dot{\gamma} \approx 0$ (Fig. 10), indicating that mixing is also due to the continuous SF mechanism rather than discontinuous CS mixing. Remarkably, the presence of free-slip conditions makes robust, efficient mixing more likely in topological mixing devices. These results confirm that the basic topology of the mixing device generates fluid mixing by enforcing separation of fluid elements impinging on the bifurcation to stretch and deform, rather than the dynamics of the flow and BCs. Hence the mixing behavior is almost fully independent of the fluid rheology and BCs.

V. CONCLUSIONS

The efficient, uniform mixing of yield stress fluids is particularly challenging due to large shear stresses involved to flow the material, eliminating conventional approaches such as turbulent flow or active stirring via, e.g., impellers. While chaotic advection represents a particularly promising method to mix such fluids (via the stretching and folding of material elements), several challenges are outstanding. First, these materials tend to yield discontinuous via slip planes, rending mixing more akin to cutting and shuffling associated with mixing of discontinuously deforming media. Second, they can invoke plastic regions under flow that involve zero fluid deformation. Third, these materials have a strong tendency to slip at wall boundaries, retarding control of flow via boundary motions. Finally, it is also desirable to develop mixing devices that mix effectively and robustly over a wide range of rheologies, so we require a class of mixer that is rheology-independent. In this study, we considered the efficacy of a class of *topological mixer*, a static mixing device that generates chaotic mixing due to its basic topology, rather than relying upon the fluid mechanics to achieve the desired deformation. We found that with minor modifications, a topological mixer based upon the 3D baker's flow is able to address these challenges very effectively. This device demonstrated rapid, efficient global mixing over a range of yield stress fluids ranging from viscous-dominated to plastic-dominant. The stretching rate (quantified by the Lyapunov exponent), mixing

rate (quantified by the rate of scalar concentration variance decay), and efficiency (measured by the proportion of deformation associated with stretching) all were independent of fluid rheology and BCs (from free-slip to no-slip). We also found that for this device, fluid stretching and folding was the dominant mixing mechanism, while cutting a shuffling played a minor role. These results provide significant insights into the kinematics of deformation of yield stress materials in such devices, and they demonstrate that a very simple, practical static mixer is capable of successfully meeting the many challenges associated with robust mixing of yield stress materials.

ACKNOWLEDGMENTS

The authors would like to thank the following companies that have sponsored aspects of this work as part of the AMIRA P1087 project "Integrated tailings management": Anglo American PLC, BASF Australia Ltd., Freeport-McMoRan Inc., Gold Fields Australasia Pty. Ltd., Outotec Pty. Ltd., Nalco-Ecolab Pty. Ltd., Newmont Mining Corp., Shell Canada Energy Ltd., and Total E&P Canada Ltd.

[1] J. M. Ottino and C. W. Macosko, An efficiency parameter for batch mixing of viscous fluids, Chem. Eng. Sci. **35**, 1454 (1980).
[2] H. Aref, Stirring by chaotic advection, J. Fluid Mech. **143**, 1 (1984).
[3] J. M. Ottino, *The Kinematics of Mixing: Stretching, Chaos, and Transport* (Cambridge University Press, Cambridge, UK, 1989).
[4] D. V. Khakhar and J. M. Ottino, Fluid mixing (stretching) by time periodic sequences for weak flows, Phys. Fluids **29**, 3503 (1986).
[5] F. Raynal and J.-N. Gence, Energy saving in chaotic laminar mixing, Int. J. Heat Mass Transf. **40**, 3267 (1997).
[6] D. R. Lester, M. Rudman, and G. Metcalfe, Low Reynolds number scalar transport enhancement in viscous and non-Newtonian fluids, Int. J. Heat Mass Transf. **52**, 655 (2009).
[7] A. Goetz, *Piecewise Isometries—An Emerging Area of Dynamical Systems* (Birkhäuser, Basel, 2003).
[8] I. C. Christov, R. M. Lueptow, and J. M. Ottino, Stretching and folding versus cutting and shuffling: An illustrated perspective on mixing and deformations of continua, Am. J. Phys. **79**, 359 (2011).
[9] R. Sturman, The role of discontinuities in mixing, Adv. Appl. Mech. **45**, 51 (2012).
[10] L. D. Smith, M. Rudman, D. R. Lester, and G. Metcalfe, Mixing of discontinuously deforming media, Chaos **26**, 023113 (2016).
[11] L. D. Smith, M. Rudman, D. R. Lester, and G. Metcalfe, Localized shear generates three-dimensional transport, Chaos: Interdisc. J. Nonlinear Sci. **27**, 043102 (2017).
[12] G. Metcalfe, M. Rudman, A. Brydon, L. J. W. Graham, and R. Hamilton, Composing chaos: An experimental and numerical study of an open duct mixing flow, AIChE J. **52**, 9 (2006).
[13] D. R. Lester, M. Rudman, G. Metcalfe, and H. M. Blackburn, Global parametric solutions of scalar transport, J. Comput. Phys. **227**, 2032 (2008).
[14] D. V. Khakhar, J. G. Franjione, and J. M. Ottino, A case study of chaotic mixing in deterministic flows: The partitioned-pipe mixer, Chem. Eng. Sci. **42**, 2909 (1987).
[15] V. V. Meleshko, O. S. Galaktionov, G. W. M. Peters, and H. E. H. Meijer, Three-dimensional mixing in Stokes flow: the partitioned pipe mixer problem revisited, Eur. J. Mech. B/Fluids **18**, 783 (1999).
[16] M. K. Singh, P. D. Anderson, and H. E. H. Meijer, Understanding and optimizing the SMX static mixer, Macromol. Rapid Commun. **30**, 362 (2009).
[17] A. D. Stroock, S. K. W. Dertinger, A. Ajdari, I. Mezić, H. A. Stone, and G. M. Whitesides, Chaotic mixer for microchannels, Science **295**, 647 (2002).

[18] D. R. Lester, G. Metcalfe, and M. G. Trefry, Is Chaotic Advection Inherent to Porous Media Flow? Phys. Rev. Lett. **111**, 174101 (2013).
[19] D. R. Lester, M. Dentz, and T. Le Borgne, Chaotic mixing in three-dimensional porous media, J. Fluid Mech. **803**, 144 (2016).
[20] P. Carrière, On a three-dimensional implementation of the baker's transformation, Phys. Fluids **19**, 118110 (2007).
[21] P. L. Boyland, H. Aref, and M. A. Stremler, Topological fluid mechanics of stirring, J. Fluid Mech. **403**, 277 (2000).
[22] E. Gouillart, J.-L. Thiffeault, and M. D. Finn, Topological mixing with ghost rods, Phys. Rev. E **73**, 036311 (2006).
[23] A. Surana, O. Grunberg, and G. Haller, Exact theory of three-dimensional flow separation. part 1. steady separation, J. Fluid Mech. **564** (2006).
[24] R. S. MacKay, Complicated dynamics from simple topological hypotheses, Philos. Trans.: Math., Phys. Eng. Sci. **359**, 1479 (2001).
[25] D. Lester, G. Metcalfe, and M. Rudman, Control mechanisms for the global structure of scalar dispersion in chaotic flows, Phys. Rev. E **90**, 022908 (2014).
[26] D. R. Lester, M. G. Trefry, and G. Metcalfe, Chaotic advection at the pore scale: Mechanisms, upscaling and implications for macroscopic transport, Adv. Water Resourc. **97**, 175 (2016).
[27] J.-M. Hertzsch, R. Sturman, and S. Wiggins, Dna microarrays: Design principles for maximizing ergodic, chaotic mixing, Small **3**, 202 (2007).
[28] S. W. Jones and H. Aref, Chaotic advection in pulsed source–sink systems, Phys. Fluids **31**, 469 (1988).
[29] M. Bercovier and M. Engelman, A finite-element method for incompressible non-newtonian flows, J. Comput. Phys. **36**, 313 (1980).